Spin echo small-angle neutron scattering using superconducting magnetic Wollaston prisms

Funama, Fumiaki; Wolf, Caitlyn M.; Weigandt, Katie; Shen, Jiazhou; Parnell, Steven R.; Li, Fankang

DOI
10.1063/5.0217884

Publication date
2024

Document Version
Final published version

Published in
Review of Scientific Instruments

Citation (APA)
Funama, F., Wolf, C. M., Weigandt, K., Shen, J., Parnell, S. R., & Li, F. (2024). Spin echo small-angle neutron scattering using superconducting magnetic Wollaston prisms. *Review of Scientific Instruments*, *95*(7), Article 073709. https://doi.org/10.1063/5.0217884

Review of
Scientific Instruments

ARTICLE

pubs.aip.org/aip/rsi

Spin echo small-angle neutron scattering using superconducting magnetic Wollaston prisms

Cite as: Rev. Sci. Instrum. 95, 073709 (2024); doi: 10.1063/5.0217884
Submitted: 7 May 2024 • Accepted: 16 June 2024 •
Published Online: 17 July 2024

View Online Export Citation CrossMark

Fumiaki Funama,[1,a)] **Caitlyn M. Wolf,**[2,b)] **Katie Weigandt,**[2,c)] **Jiazhou Shen,**[3,4,5,d)]
Steven R. Parnell,[6,7,e)] **and Fankang Li**[1,f)]

AFFILIATIONS

[1] Neutron Technologies Division, Oak Ridge National Laboratory, Oak Ridge, Tennessee 37830, USA
[2] NIST Center for Neutron Research, National Institute of Standards and Technology, Gaithersburg, Maryland 20899, USA
[3] Department of Physics, Indiana University, Bloomington, Indiana 47405, USA
[4] Indiana University Center for the Exploration of Energy and Matter, Bloomington, Indiana 47408, USA
[5] Indiana University Quantum Science and Engineering Center, Bloomington, Indiana 47408, USA
[6] ISIS, Rutherford Appleton Laboratory, Chilton, Oxfordshire OX11 0QX, United Kingdom
[7] Faculty of Applied Sciences, Delft University of Technology, Mekelweg 15, 2629JB Delft, The Netherlands

[a)] **Electronic mail:** funamaf@ornl.gov
[b)] **Electronic mail:** caitlyn.wolf@nist.gov
[c)] **Electronic mail:** kathleen.weigandt@nist.gov
[d)] **Current address:** Laboratory for Neutron Scattering and Imaging, Paul Scherrer Institut, 5232 Villigen, Switzerland.
Electronic mail: jiazhou.shen@psi.ch
[e)] **Electronic mail:** steven.parnell@stfc.ac.uk
[f)] **Author to whom correspondence should be addressed:** frankli@ornl.gov

ABSTRACT

We show the implementation of superconducting magnetic Wollaston prisms for spin echo small-angle neutron scattering. Two calibration methods for the spin echo length are presented: one utilizing spin echo modulated small-angle neutron scattering and the other based on the neutron refraction by quartz wedge crystals. Our experimental results with polystyrene nano-particle colloids showcase the system's efficacy in measuring both dilute and concentrated colloidal systems. Additionally, investigations into the pore diameter and pitch of a nano-porous alumina membrane demonstrate its capability in analyzing nano-porous materials. Furthermore, we discuss potential optimizations to further extend the accessible spin echo length.

I. INTRODUCTION

Spin echo small-angle neutron scattering (SESANS) is a method that surpasses the resolution of conventional small-angle neutron scattering (SANS) by extending the lowest measurable momentum transfer. Instead of directly measuring the momentum transfer of a neutron beam by measuring its scattering angle, SESANS encodes the momentum transfer into Larmor phase through precisely controlled magnetic fields. The Larmor phase of the sacttered neutron beam is given by the following equation:[1]

$$\Phi = \vec{\delta} \cdot \vec{Q}, \qquad (1)$$

where δ represents the spin echo length (SEL), determining the lowest resolvable momentum transfer. With encoding direction $\vec{\delta}$ along with the momentum transfer $\vec{Q}$, it provides us with the capability to encode Q into the Larmor phase Φ, enabling SESANS to perform a Hankel transformation of $I(Q)$ to measure the correlation functions in real space rather than in the reciprocal space of SANS.[2] Quantum mechanically, the SEL corresponds to the physical separation between the two neutron spin states within the SESANS apparatus. Various encoding apparatus, such as magnetized Permalloy foils,[3–5,38] neutron resonance spin flippers (RSFs),[3,6,7] and room temperature magnetic Wollaston prisms (MWPs),[8–10] have been developed for SESANS, all involving the physical inclination of the magnetic field boundary relative to the neutron beam to achieve the transverse encoding of the scattering sensitivity to $\vec{Q}$.

This report focuses on implementing SESANS using superconducting MWPs. While the technical details of a superconducting MWP have been shown in Refs. 11 and 39, it is comprised of two adjacent triangular magnetic prisms with opposite fields across the hypotenuse. A MWP can spatially split a superposition state of two neutron spin states due to their different magnetic potentials. While room temperature MWPs have been utilized for SESANS, their performance is hindered by magnetic field aberrations arising from the required precision in wire positioning,[12] neutron attenuation, and parasitic scattering. Superconducting MWPs, previously used in Larmor diffraction,[13,14] inelastic neutron spin echo (INSE),[15] and spin echo modulated small-angle scattering (SEMSANS)[16–18] experiments, offer advantages including high spin transport efficiency, minimal neutron attenuation, reduced parasitic scattering, and a higher magnetic field.

This paper presents the implementation of superconducting MWPs for SESANS experiments, together with two calibration methods for the SEL. We will also show its applications in the characterization of polystyrene nano-particle (PSNP) colloids and nano-porous alumina membranes. Finally, potential improvements to extend the maximum SEL are discussed.

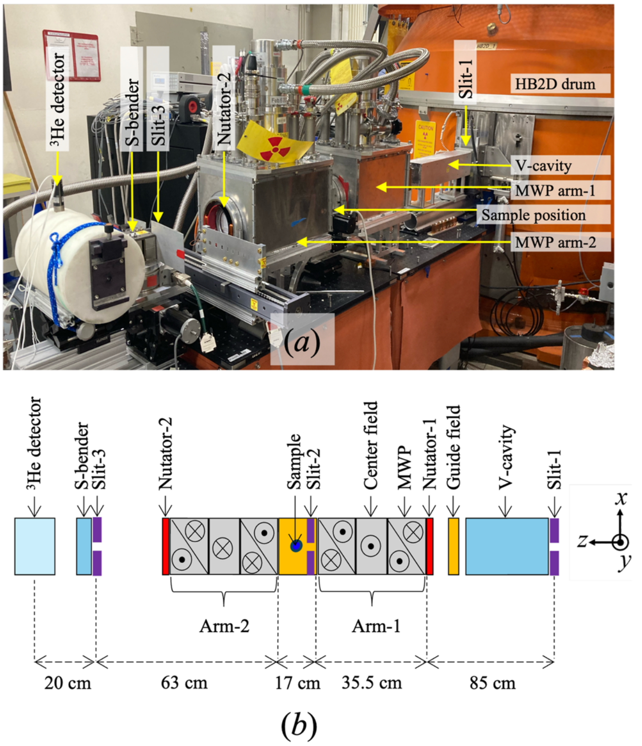

FIG. 1. SESANS experimental setup at the HB2D beamline of HFIR: (a) a comprehensive view of the SESANS instrument setup. (b) a schematic diagram illustrating the key components and structures. The top view of the instrument is shown. Each MWP arm consists of two MWPs and a rectangular center field. All guide fields are in the negative direction along the y axis. Both fields in Nutator-1 and Nutator-2 are in the positive direction along the x axis.

II. SESANS SETUP

The SESANS experiments were conducted at the HB2D polarized test beamline of the High Flux Isotope Reactor (HFIR).[19] HB2D utilizes a highly oriented pyrolytic graphite (HOPG) monochromator set at a take-off angle of 78.6°. A 100-mm-thick beryllium filter, maintained at room temperature, effectively transmits neutrons with a wavelength of 4.25 Å while minimizing the high-order reflections from the monochromator. Figure 1 illustrates the experimental setup. The details of the neutron optics components can be found in Ref. 20. The monochromatic beam is polarized using a supermirror V-cavity and then guided through a series of magnetic fields to maintain the polarization. Before entering the superconducting MWPs, a magnetic nutator performs a $\pi/2$ flip, initiating the Larmor precession in the x-z plane within the MWPs. Enclosed within a vacuum chamber, the two MWPs are separated by a rectangular center field. Magnetic fields within the two arms on either side of the sample are identical but opposite in direction. The polarization vector component is selected and analyzed using an additional nutator and a polarizing S-bender. A shielded ^{3}He pencil detector is used for the detection of the neutron beam.

To determine the beam polarization, we scan the center field (B_c) in MWP arm-1, resulting in a sinusoidal oscillation of the neutron intensity described by $i(B_c) = a\sin(\omega B_c) + i_0$, where a, ω, and i_0 are the amplitude, the frequency, and the shim intensity of the sinusoidal oscillation. The polarization is then calculated as $P = \frac{a}{i_0}$. To prevent depolarization near the sample, a weak magnetic guide field of ~5 G is applied in the negative direction of the y axis. The divergence of the incoming beam at the sample position is given by Slit-1 (12.7×12.7 mm^2) and a pinhole slit of Slit-2 with a diameter of 6 mm. The maximum divergence of the scattered beam and hence Q range is constrained by Slit-3, positioned 71.5 cm from the sample, with dimensions of 30×30 mm^2. This compact instrument has a total length of ~2.2 m.

To eliminate the contributions from the neutron wavelength (λ), sample thickness (t), and instrumental artifacts, the polarization of the beam is measured both without (P_0) and with a sample (P), allowing for the calculation of the normalized scattering correlation function denoted as $\frac{\ln(P/P_0)}{\lambda^2 t}$. The SEL δ is determined by the equation

$$\delta = cBL\lambda^2 \cot\theta. \tag{2}$$

In this context, $c = \frac{\gamma m}{\pi h} = 1.476 \times 10^{10}$ G^{-1} m^{-2}, where c represents a constant, γ is the neutron gyromagnetic ratio, m is the neutron mass, and h is Planck's constant. The magnetic field within the MWPs is denoted by B, while L signifies the separation between the two MWPs in each arm, and θ represents the angle between the hypotenuse of the MWP and the beam direction. For the superconducting MWPs, L and θ are set to 0.21 m and 45°, respectively. The SEL is scanned by adjusting the magnetic field inside the MWP (B), achieved by varying the applied current I of the MWPs for each arm. Equation (2) indicates that calibrating the SEL necessitates calibration of the magnetic field inside the MWPs, a topic addressed in Sec. III.

III. CALIBRATION OF THE SPIN ECHO LENGTH

Different approaches have been employed to calibrate SESANS instruments, such as using optical gratings for Offspec at ISIS[21,22] and refraction from aluminum wires for SESANS at TU-Delft.[23] However, these methods employs long length scale sample structures, posing challenges in calibrating shorter SEL in the range of a few tens to hundreds of nm. Here, we introduce two additional approaches to calibrate the magnetic field inside the MWPs and hence the SEL. The first method involves spin echo modulated small angle neutron scattering (SEMSANS) to modulate the beam profile to generate an intensity pattern on the detector. By precisely measuring the period of this pattern, the magnetic field can be calibrated. This technique does not require a sample but necessitates a high-resolution position-sensitive detector (PSD). Alternatively, the second approach utilizes the refraction of a neutron beam as it passes through an optical quartz wedge. This deflection introduces a well-defined momentum transfer, allowing for precise calibration of the SEL and magnetic field according to Eq. (1), provided that the Larmor phase can be accurately measured. In this case, a regular integrating pencil detector is sufficient.

These experiments were performed at the cold neutron polarization development beamline at CG-4B in HFIR. A monochromatic neutron beam with a wavelength of 5.5 Å, which is achieved by reflecting the neutrons from a hot-pressed silicon monochromator, was used.

A. Calibration using SEMSANS signals

SEMSANS is a variant of the SESANS technique that induces spatial intensity modulations.[24] In this configuration, the MWPs within the second arms are subjected to higher magnetic fields, satisfying the SEMSANS condition to generate spatial intensity modulations with high contrast, independent of beam divergence. The modulation period T_M of the SEMSANS signals is determined as follows:

$$T_M = \frac{\tan(\theta)}{2c\lambda(B_2 - B_1)} = \frac{\tan(\theta)}{2c\lambda\alpha(I_2 - I_1)}. \tag{3}$$

Here, B_1 and B_2 represent the magnetic fields, written as αI_1 and αI_2, respectively, where α, I_1, and I_2 denote the magnetic field per current inside the MWPs and the applied current in MWPs for the first and second arms, respectively. By measuring the SEMSANS period with a high-resolution PSD, the magnetic field and hence SEL can be determined. To measure the beam modulation, a scintillator-based Timepix3 detector was utilized, offering a spatial resolution of 0.2 mm with a LiF:ZnS(Ag) scintillator.[25]

In Fig. 2(a), SEMSANS periods are plotted against $I_2 - I_1$. All error bars in the experimental data in this paper represent one standard deviation. As expected from Eq. (3), the period T_M demonstrates an inverse relationship with $I_2 - I_1$. The maximum I_2 value recorded in this measurement was 10 A. The observed minimum period is 0.62 ± 0.002 mm when $I_2 - I_1$ is 2.8 A. Figure 2(b) depicts α calculated using T_M as a function of $I_2 - I_1$. Error values are derived from the fitting errors of T_M. Notably, α remains nearly constant regardless of $I_2 - I_1$, with any slight differences potentially attributable to non-linearity of the magnetic permeability of the materials used in the MWPs. The obtained α values, averaged across all results, are 35.06 ± 0.04 G/A.

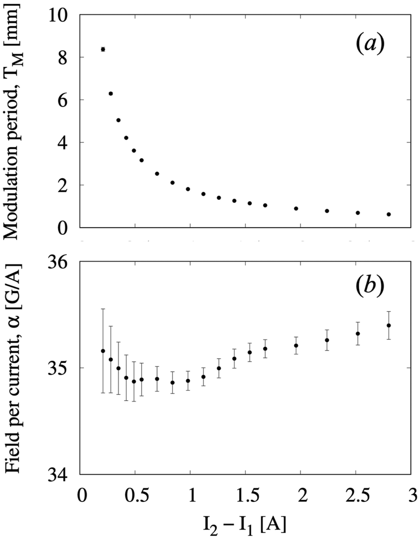

FIG. 2. (a) The intensity modulation period T_M of SEMSANS signals as a function of $I_2 - I_1$. (b) Magnetic field per current α of the MWPs calculated using T_M and Eq. (3).

B. Calibration using quartz wedge crystal

In SESANS, the Larmor phase accumulated by the neutron spin throughout the setup is given by Eq. (1). For a neutron beam passing through a crystal with a wedge shape, the induced momentum transfer of the neutron beam has been calculated by Rekveldt *et al.*[26] as $Q = -\frac{2\rho\lambda}{\sin(2\phi)}$ for $\phi \ll 1$, where ϕ is the inclination angle and ρ is the coherent scattering length density of quartz, taking a value of 4.183×10^{-6} Å $^{-2}$. In a quantum picture, this is also equivalent to the path phase difference between the two spin states.[27,28] The setup used for this experiment is shown in Fig. 3(a), and the Larmor phase for the refracted neutron is determined as follows:

$$\begin{aligned}\Phi &= -\frac{4\rho\lambda\delta}{\sin(2\phi)} \\ &= -\frac{4\gamma m\lambda^3\rho L}{\pi h} \cdot \frac{\cot(\theta)}{\sin(2\phi)} \cdot B(I).\end{aligned} \tag{4}$$

Since all parameters in Eq. (4) except the magnetic field (B) are known, measuring the Larmor phase Φ allows for the calibration of the magnetic field and hence the SEL.

Figure 3(b) presents the measured Larmor phase as a function of the current inside the MWPs for two inclination angles, $\phi = +3.1°$ and $\phi = -3.1°$. To mitigate instrumental error, the Larmor phase without the quartz wedge ($\phi = 0$) is utilized as a reference and subtracted accordingly. The Larmor phase data are fitted with a linear function, and the slope κ is indicated in the figure. Utilizing this slope, the magnetic field per current can be extracted as 34.6 G/A for $\phi = +3.1°$ and 35.8 G/A for $\phi = -3.1°$. This corresponds to

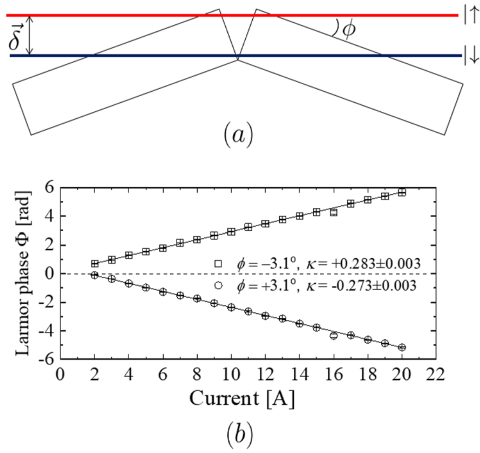

FIG. 3. (a) Schematic of the SESANS calibration setup utilizing a quartz wedge with ϕ indicating the inclination angle relative to the beam direction. Two lines of different colors represent the two spin states. The two wedges can be rotated or translated independently from each other. (b) The Larmor phase is measured as a function of current inside the MWPs by scanning the guide field between the MWPs. The data points have been fitted linearly with a slope of κ.

a SEL of 32.14 nm/A and 33.25 nm/A, respectively. The slight discrepancy between the positive and negative values may arise from the angular misalignment between the MWPs and the quartz wedge. The average value of the two measurement results is 35.2 G/A, which is almost the same as the result obtained with the SEMSANS signals presented in the previous section. This value also agrees with the field simulated with the finite element analysis software MagNet,[29] which yields a value of 36.4 G/A.

IV. SESANS EXPERIMENTAL RESULTS

A. Polystyrene nano-particle colloids

To assess the performance of the SESANS setup, carboxyl-functionalized polystyrene nano-particle (PSNP) colloids with varying sizes and concentrations are examined.[30] The PSNP colloids at nominal particle diameters of 50, 101, and 198 nm were purchased from Bangs Laboratories, Inc.[31] The nominal diameter represents a hydrodynamic diameter determined by dynamic light scattering (DLS). Solvent exchange from water to heavy water was achieved by ultra-filtration, while the concentration of sodium dodecyl sulfate was maintained at 0.0035 M. The nominal volume fractions of the samples were estimated by the mass fraction of the particles in water provided by the supplier and by tracking the mass of the colloid during the ultra-filtration solvent exchange. The prepared samples were loaded into quartz banjo cells with a path length of 2 mm.

Figure 4 displays the results obtained with the PSNP colloids at nominal particle diameters of 50 and 198 nm and a nominal volume fraction of 5%. The SELs shown in Fig. 4 are calculated using the calibrated magnetic field per current value of 35 G/A. The curves plateau as the SEL reaches the maximum correlation length within the sample. Particle diameters for each colloid are determined through fitting with a dilute sphere model.[2] The evaluated diameters are 50.7 ± 2.9 nm and 185.4 ± 2.3 nm, respectively, which agree well with the nominal diameters. Neutrons are sensitive to the particle only, so the evaluated diameters may be slightly smaller than the nominal (hydrodynamic) particle diameters. These experimental findings underscore the capability of SESANS to measure dilute colloidal systems.

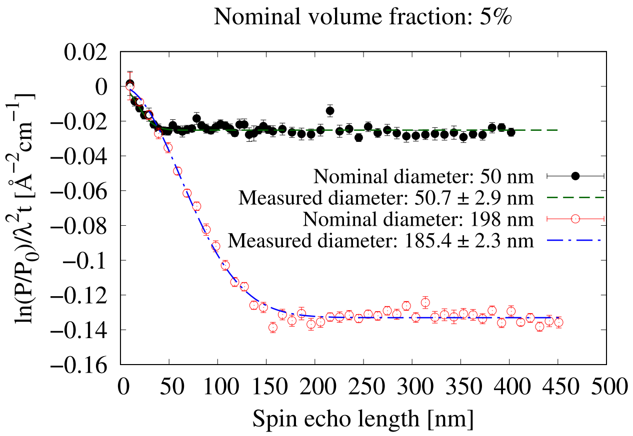

FIG. 4. Normalized scattering correlation functions of the PSNP colloids with identical nominal volume fractions of 5% but different particle sizes.

Three PSNP colloids with different volume fractions of 5%, 10%, and 20% and a nominal particle size of 101 nm were measured, and the normalized scattering correlation functions are shown in Fig. 5. As the concentration increases, the functions exhibit greater oscillations indicative of inter-particle correlations and interactions. Therefore, these results are fitted using the sphere form factor and the Hayter–Pen-fold Mean Spherical Approximation (MSA) structure factor from SasView,[32,33] which are appropriate for charged spheres. During these fits, the scattering length density of the PSNP and D_2O solvent, the charge on the sphere, temperature, concentration of the salt, and dielectric constant of the solvent were fixed as

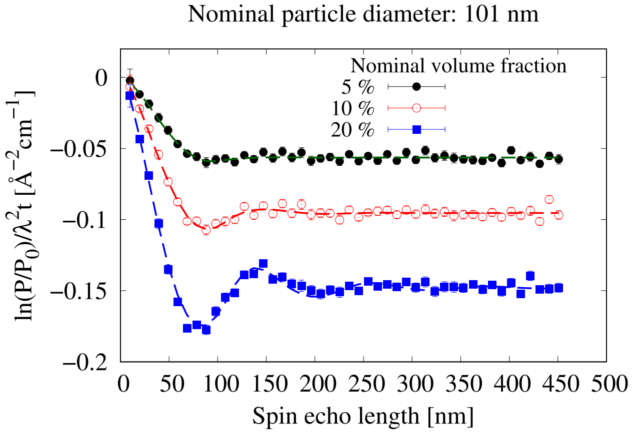

FIG. 5. Normalized scattering correlation functions of the PSNP colloids with identical particle sizes but varying concentrations yield volume fractions of 3.6 ± 3.2%, 7.9 ± 1.3%, and 18.2 ± 0.6% for nominal volume fractions of 5%, 10%, and 20%, respectively.

1.4 (10^{-6}/Å^2), 6.3 (10^{-6}/Å^2), 1 (e), 296 (K), 0.0035 (M), and 79.755, respectively.

From the 5% colloid, the sphere diameter is determined to be 102 ± 2 nm, consistent with the nominal particle diameter. The volume fractions of $3.6 \pm 3.2\%$, $7.9 \pm 1.3\%$, and $18.2 \pm 0.6\%$ are obtained for the 5%, 10%, and 20% colloids, respectively. The obtained volume fractions are slightly smaller than the nominal volume fractions. This might be due to an error in estimating the concentration during the ultra-filtration solvent exchange. Nevertheless, these experimental findings clearly demonstrate the capability of SESANS experiments with superconducting MWPs to evaluate the volume fractions of concentrated colloidal systems.

B. Nano-porous alumina membrane

A nano-porous alumina membrane obtained from SmartMembranes was also measured.[34] This membrane comprises round cylindrical pores with a diameter of 45 nm and a pore length of 150 μm. The pores are arranged hexagonally within multi-grains of alumina. The supplier provides a nominal pore pitch of $p_n = 125$ nm, measured via scanning electron microscopy (SEM). Figure 6 shows the SESANS experimental data for the membrane as well as the SEM image provided by the supplier. The strongly ordered structure of the membrane with the pits can be expressed with these models, considering the multi-grain structure in the sample. A model with a core–shell–sphere form factor and a Percus–Yevick structure factor is employed to fit the experimental results using SASview.[35,36] A core diameter of (55 ± 17) nm is determined, aligning with the supplier's nominal value. The obtained shell thickness is 37.4 ± 9 nm, which also agrees with an estimated thickness calculated with a nominal pore pitch and diameter, *i.e.*, $(125 - 45)/2$ nm = 40 nm. In Fig. 6, as SESANS is a one-dimensional technique, the oscillation period of the normalized scattering correlation function T denotes the projection of the next nearest-neighbor toward the encoding direction, which is given by $T = p\sin(60^\circ)$ as shown in the Fig. 6. Therefore, with $T = 112\pm\ 1$ nm obtained from the fitting, the calculated pore pitch can be calculated to be $p = 129 \pm 1$ nm, which is close to the nominal pore pitch provided by the supplier ($p_n = 125$ nm). The slight deviation from the nominal value may stem from methodological differences, as SEM measurements probe a smaller sampling footprint than the SESANS measurements. Nevertheless, these experimental findings underscore the capability of evaluating nano-porous materials using SESANS with superconducting MWPs.

V. POTENTIAL OPTIMIZATION OF THE MWPS FOR SESANS

The SESANS setup described in this report has a shorter accessible length scale compared to established SESANS instruments like Larmor at ISIS and SESANS at TU-Delft, due to some of the physical parameters of the MWPs being optimized for different applications. The implementation of SESANS and its use in measuring correlation functions show promising progress. The SESANS setup reported here would benefit from further optimization, which may involve reducing the hypotenuse angle, increasing the distance between the MWPs, and employing neutrons with a longer wavelength of 10 Å. Additionally, increasing the strength of the magnetic field where the superconducting film penetration occurs could further improve performance.[37] As a result, an overall increase of up to 50 times in SEL could be achieved with all parameters fully optimized. This advancement could potentially enable SELs of about 20 μm, similar to those of the Larmor instrument at ISIS and the SESANS instrument at TU-Delft. Additionally, the shorter sample-to-detector distance with MWPs enables measurement of scattering with a larger scattering angle, which is beneficial for obtaining accurate experimental results, particularly in the short SEL range below a few hundred nm.[6]

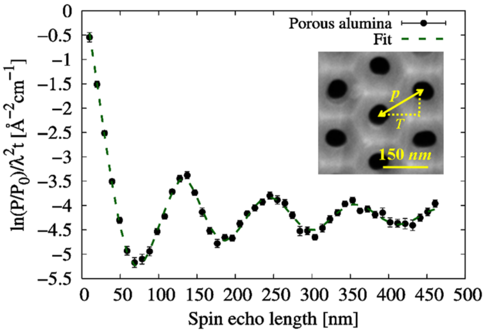

FIG. 6. Normalized scattering correlation function of a nano-porous alumina membrane. The result is fitted with the core–shell–sphere and Percus–Yevick models for form and structure factors, respectively. The inset is the SEM image provided by the supplier. The T shows the projection of the distance to the next nearest-neighbor toward the encoding direction, and p is the pore pitch of the membrane.

VI. CONCLUSION

Our study highlights the effectiveness of superconducting MWPs for SESANS experiments. We introduced calibration methods utilizing SEMSANS signals and quartz wedge crystals, demonstrating that the magnetic field per current of the MWPs is ~35 G/A. Results from dilute and concentrated PSNP colloids illustrate the capability to determine particle sizes and volume fractions. Additionally, experimental findings on nano-porous alumina membranes show the ability to evaluate pore size and pitch in nanoporous materials. Finally, we discussed the potential enhancement of achievable SELs with optimized MWPs and their arms for SESANS applications.

ACKNOWLEDGMENTS

We would like to extend our gratitude to Dr. Wim Bouwman (TU-Delft) for his insightful discussions on nano-porous alumina samples. The authors are also grateful to Doug Kyle (ORNL) for his support of the experiments. We would like to acknowledge Gary Taufer and Ray Gregory (ORNL) for the development of instrument control systems to automate the measurements. We appreciate Mike Harrington and Hugh Harvey (ORNL) for the hardware support. We are also grateful to David Sexton (ORNL) for his machining support. This work benefited from the use of the SasView application, originally developed under NSF Award No. DMR-0520547. SasView contains code developed with funding from the European Union's Horizon 2020 research and innovation program under the SINE2020 project, Grant Agreement No. 654000. This work was supported by the U.S. Department of Energy (DOE), Office of Science, Office of Basic Energy Sciences, Early Career Research Program Award No. (KC0402010), under Contract No. DE-AC05-00OR22725. K.W. and C.M.W. were supported by National Institute of Standards and Technology (NIST) funding. This research used resources at the High Flux Isotope Reactor, a DOE Office of Science User Facility operated by the Oak Ridge National Laboratory.

Certain commercial equipment or software are identified in this paper to foster understanding. Such identification does not imply recommendation or endorsement by the National Institute of Standards and Technology, nor does it imply that the equipment or software identified is necessarily the best available for the purpose.

AUTHOR DECLARATIONS

Conflict of Interest

The authors have no conflicts to disclose.

Author Contributions

Fumiaki Funama: Conceptualization (equal); Data curation (equal); Formal analysis (equal); Investigation (equal); Methodology (equal); Software (equal); Validation (equal); Visualization (equal); Writing – original draft (equal). **Caitlyn M. Wolf**: Formal analysis (equal); Resources (equal); Validation (equal); Writing – review & editing (equal). **Katie Weigandt**: Formal analysis (equal); Resources (equal); Validation (equal). **Jiazhou Shen**: Investigation (equal). **Steven R. Parnell**: Validation (equal); Writing – review & editing (equal). **Fankang Li**: Conceptualization (equal); Data curation (equal); Formal analysis (equal); Funding acquisition (equal); Investigation (equal); Methodology (equal); Project administration (equal); Resources (equal); Software (equal); Supervision (equal); Validation (equal); Writing – review & editing (equal).

DATA AVAILABILITY

The data that support the findings of this study are available from the corresponding author upon reasonable request.

REFERENCES

[1] R. Pynn, M. Fitzsimmons, W. Lee, P. Stonaha, V. Shah, A. Washington, B. Kirby, C. Majkrzak, and B. Maranville, "Birefringent neutron prisms for spin echo scattering angle measurement," Physica B **404**, 2582–2584 (2009).

[2] R. Andersson, L. F. van Heijkamp, I. M. de Schepper, and W. G. Bouwman, "Analysis of spin-echo small-angle neutron scattering measurements," J. Appl. Crystallogr. **41**, 868–885 (2008).

[3] M. T. Rekveldt, J. Plomp, W. G. Bouwman, W. H. Kraan, S. Grigoriev, and M. Blaauw, "Spin-echo small angle neutron scattering in delft," Rev. Sci. Instrum. **76**, 033901 (2005).

[4] W. Kraan, J. Plomp, T. Krouglov, W. Bouwman, and M. T. Rekveldt, "Ferromagnetic foils as monochromatic π flippers for application in spin-echo sans," Physica B **335**, 247–249 (2003).

[5] T. Wang, X. Tu, Y. Wang, X. Li, J. Gong, and G. Sun, "Design and simulations of spin-echo small angle neutron scattering spectrometer at CMRR," Nucl. Instrum. Methods Phys. Res., Sect. A **1024**, 166041 (2022).

[6] R. Dalgliesh, S. Langridge, J. Plomp, V. De Haan, and A. Van Well, "Offspec, the ISIS spin-echo reflectometer," Physica B **406**, 2346–2349 (2011).

[7] S. Parnell, R. Dalgliesh, N. Steinke, J. Plomp, and A. Van Well, "RF neutron spin flippers in time of flight Spin-Echo Resolved Grazing Incidence Scattering (SERGIS)," J. Phys.: Conf. Ser. **1021**, 012040 (2018).

[8] R. Pynn, M. Fitzsimmons, W. Lee, V. Shah, A. Washington, P. Stonaha, and K. Littrell, "Spin echo scattering angle measurement at a pulsed neutron source," J. Appl. Crystallogr. **41**, 897–905 (2008).

[9] S. Parnell, A. Washington, K. Li, H. Yan, P. Stonaha, F. Li, T. Wang, A. Walsh, W. Chen, A. Parnell *et al.*, "Spin echo small angle neutron scattering using a continuously pumped 3he neutron polarisation analyser," Rev. Sci. Instrum. **86**, 023902 (2015).

[10] A. Washington, X. Li, A. B. Schofield, K. Hong, M. Fitzsimmons, R. Dalgliesh, and R. Pynn, "Inter-particle correlations in a hard-sphere colloidal suspension with polymer additives investigated by Spin Echo Small Angle Neutron Scattering (SESANS)," Soft Matter **10**, 3016–3026 (2014).

[11] F. Li, S. R. Parnell, W. A. Hamilton, B. B. Maranville, T. Wang, R. Semerad, D. V. Baxter, J. T. Cremer, and R. Pynn, "Superconducting magnetic Wollaston prism for neutron spin encoding," Rev. Sci. Instrum. **85**, 053303 (2014).

[12] P. Stonaha, J. Hendrie, W. Lee, and R. Pynn, "Neutron spin evolution through broadband current sheet spin flippers," Rev. Sci. Instrum. **84**, 105113 (2013).

[13] F. Li, H. Feng, A. N. Thaler, S. R. Parnell, W. A. Hamilton, L. Crow, W. Yang, A. B. Jones, H. Bai, M. Matsuda *et al.*, "High resolution neutron Larmor diffraction using superconducting magnetic Wollaston prisms," Sci. Rep. **7**, 865 (2017).

[14] F. Li, H. Feng, A. N. Thaler, S. R. Parnell, L. Crow, M. Matsuda, F. Ye, T. Kimura, J. A. Fernandez-Baca, and R. Pynn, "New capabilities in high-resolution neutron Larmor diffraction at ORNL," J. Appl. Crystallogr. **51**, 584–590 (2018).

[15] F. Li, J. Shen, S. R. Parnell, A. N. Thaler, M. Matsuda, T. Keller, O. Delaire, R. Pynn, and J. A. Fernandez-Baca, "High-resolution phonon energy shift measurements with the inelastic neutron spin echo technique," J. Appl. Crystallogr. **52**, 755–760 (2019).

[16] F. Li, N.-J. Steinke, R. M. Dalgliesh, A. L. Washington, J. Shen, R. Pynn, and S. R. Parnell, "Probing magnetic correlations with spin-echo modulated small angle neutron scattering (SEMSANS)," Nucl. Instrum. Methods Phys. Res., Sect. A **1014**, 165705 (2021).

[17] F. Li, S. R. Parnell, R. Dalgliesh, A. Washington, J. Plomp, and R. Pynn, "Data correction of intensity modulated small angle scattering," Sci. Rep. **9**, 8563 (2019).

[18] J. Schmitt, J. J. Zeeuw, J. Plomp, W. G. Bouwman, A. L. Washington, R. M. Dalgliesh, C. P. Duif, M. A. Thijs, F. Li, R. Pynn *et al.*, "Mesoporous silica formation mechanisms probed using combined spin–echo modulated small-angle neutron scattering (SEMSANS) and small-angle neutron scattering (SANS)," ACS Appl. Mater. Interfaces **12**, 28461–28473 (2020).

[19] L. Crow, W. Hamilton, J. Zhao, and J. Robertson, "The HB-2D polarized neutron development beamline at the high flux isotope reactor," J. Phys.: Conf. Ser. **746**, 012010 (2016).

[20] H. Börner, J. Brown, C. Carlile, R. Cubitt, R. Currat, A. Dianoux, B. Farago, A. Hewat, J. Kulda, E. Lelièvre-Berna *et al.*, *Neutron Data Booklet* (ILL: Grenoble, France, 2003).

[21] M. Trinker, E. Jericha, W. Bouwman, R. Loidl, and H. Rauch, "Analysis of artificial silicon microstructures by ultra-small-angle and spin-echo small-angle neutron scattering," Nucl. Instrum. Methods Phys. Res., Sect. A **579**, 1081–1089 (2007).

[22] J. Plomp, V. De Haan, R. Dalgliesh, S. Langridge, and A. Van Well, "Spin-echo length calibration of OffSpec," Physica B **406**, 2354–2356 (2011).

[23] J. Plomp, J. Barker, V. De Haan, W. Bouwman, and A. van Well, "Neutron refraction by cylindrical metal wires," Nucl. Instrum. Methods Phys. Res., Sect. A **574**, 324–329 (2007).

[24] W. G. Bouwman, C. P. Duif, and R. Gähler, "Spatial modulation of a neutron beam by Larmor precession," Physica B **404**, 2585–2589 (2009).

[25] F. Funama, S.-A. Chong, M. Loyd, K. J. Gofron, Y. Zhang, S. J. Kuhn, C. Zhang, M. R. Fitzsimmons, A. Khaplanov, B. Vacaliuc *et al.*, "Scintillator-based timepix3 detector for neutron spin-echo techniques using intensity modulation," Rev. Sci. Instrum. **95**, 033304 (2024).

[26] M. T. Rekveldt, W. G. Bouwman, W. H. Kraan, and J. Plomp, "Neutron refraction and transmission studied by SESANS," Physica B **350**, E791–E794 (2004).

[27] J. Shen, S. J. Kuhn, R. M. Dalgliesh, V. de Haan, N. Geerits, A. A. Irfan, F. Li, S. Lu, S. R. Parnell, J. Plomp *et al.*, "Unveiling contextual realities by microscopically entangling a neutron," Nat. Commun. **11**, 930 (2020).

[28] S. Kuhn, S. McKay, J. Shen, N. Geerits, R. Dalgliesh, E. Dees, A. Irfan, F. Li, S. Lu, V. Vangelista *et al.*, "Neutron-state entanglement with overlapping paths," Phys. Rev. Res. **3**, 023227 (2021).

[29] Siemens Software, Simcenter MAGNET, Magnet, 2024 https://plm.sw.siemens.com/en-US/simcenter/electromagnetics-simulation/magnet/.

[30] C. M. Wolf, P. Bajcsy, W.-R. Chen, R. M. Dalgliesh, M. C. Daugherty, L. de Campo, F. Funama, L. He, M. Huber, D. Jacobson, P. Kienzle, Y. Kim, H. King, N. Klimov, J. LaManna, F. Li, A. M. Long, R. Murphy, G. Nagy, S. M. Robinson, P. Sathe, G. N. Smith, A. Sokolova, S. Vogel, E. B. Watkins, Y. Zhang, D. Hussey, and K. Weigandt, "Small-angle scattering and dark field imaging for validation of a new neutron far-field interferometer," (unpublished).

[31] Functionalized polystyrene https://www.bangslabs.com/products/polystyrene-microspheres/functionalized-polystyrene/; accessed March 21, 2024.

[32] M. Doucet, J. H. Cho, G. Alina, J. Bakker, W. Bouwman, P. Butler, K. Campbell, M. Gonzales, R. Heenan, A. Jackson *et al.* (2017). "SasView version 4.1," Zenodo. http://www.sasview.org

[33] J. H. Bakker, A. L. Washington, S. R. Parnell, A. A. Van Well, C. Pappas, and W. G. Bouwman, "Analysis of SESANS data by numerical Hankel transform implementation in SasView," J. Neutron Res. **22**, 57–70 (2020).

[34] SmartMembranes http://www.smartmembranes.de/en/products/nanoporous-alumina/; accessed March 21, 2024.

[35] J. K. Percus and G. J. Yevick, "Analysis of classical statistical mechanics by means of collective coordinates," Phys. Rev. **110**, 1 (1958).

[36] M. Kotlarchyk and S.-H. Chen, "Analysis of small angle neutron scattering spectra from polydisperse interacting colloids," J. Chem. Phys. **79**, 2461–2469 (1983).

[37] J. Shen, *Quantum Description and Applications of Neutron Spin-Echo Devices* (Indiana University, 2021).

[38] R. Pynn, M. R. Fitzsimmons, H. Fritzsche, M. Gierlings, J. Major, and A. Jason, "Neutron spin echo scattering angle measurement (SESAME)," Rev. Sci. Instrum. **76**, 053902 (2005).

[39] F. Li, S. Parnell, T. Wang, D. Baxter, and R. Pynn, "Magnetic field optimization and design of a superconducting neutron Wollaston prism," J. Phys.: Conf. Ser. **711**, 012015 (2016).